UNIVERSITY OF CALIFORNIA
SANTA CRUZ

HIGH SPATIAL RESOLUTION DEDICATED HEAD AND NECK POSITRON EMISSION TOMOGRAPHY SYSTEM BASED ON CADMIUM ZINC TELLURIDE DETECTORS

A thesis submitted in partial satisfaction of the
requirements for the degree of

MASTER OF SCIENCE

in

ELECTRICAL AND COMPUTER ENGINEERING

by

Yuli Wang

June 2021

The Thesis of Yuli Wang is approved:

Professor Shiva Abbaszadeh, Chair

Professor Holger Schmidt

Professor Sara Abrahamsson

Quentin Williams
Vice Provost and Dean of Graduate Studies

Table of Contents

List of Figures

List of Tables

Abstract

High spatial resolution dedicated head and neck Positron emission tomography system based on cadmium zinc telluride detectors

by

Yuli Wang

Current head and neck cancer diagnosis and treatment planning suffers from poor spatial resolution of whole-body positron emission tomography (PET) scans. A dedicated two-panel positron emission tomography system is developed to improve head and neck cancer management. The two-panel design was selected considering human factors to assist with patient comfort by removing detectors closer to eyesight of the patient and assist with optimal workflow in the PET environment. The proposed system will be the first head and neck scanner to exhibit features as small as 1 mm with high photon sensitivity, enabled by the use of high energy and spatial resolution properties of cadmium zinc telluride (CZT) crystals. The panels will be used right after standard PET, using the same bed and FDG dose. A novel event recovery scheme based on the 3D position sensitive cross-strip crystals is developed to recover multiple interaction photon events, reject random events, and significantly increase the photon sensitivity of the system. A penalized maximum-likelihood method with an image-based resolution model incorporated into a regularization term was considered to improve limited angle artifacts in reconstructed images of two panels using the whole-body image as prior.

To my parents, for their love and support

Acknowledgments

It is an amazing experience for me to perform the research work presented here at Radiological Instrumentation Laboratory in the past two years.

I would firstly express my deep gratitude and appreciate to my advisor Prof. Shiva Abbaszadeh, who has been a great teacher, mentor as well as the most trustworthy source of guidance and support through this project. I am especially grateful to her for giving me the opportunities and resources to work on many great ideas and always encouraging me to do the things I want to do.

I would also like to thank the members of my thesis reading committee, Prof. Holger Schmidt and Prof. Sara Abrahamsson, for your support and informative suggestions.

I would like to thank all my colleagues at the Radiological Instrumentation Laboratory, both current and former members, for their friendship, help, inspirations and encouragement.

I would like to acknowledge funding support from the National Institute of Biomedical Imaging and Bioengineering of the National Institutes of Health under Award Number R01EB028091.

Lastly, I would like to thank my family. Their love and care for me is the biggest source of my courage and energy that supported me to pursue my dream. I would also like to thank my friends, who brought a lot of happiness to my life and gave me so much help.

Chapter 1

Introduction

Positron emission tomography (PET) is an in-vivo medical imaging modality that enables the early cancer (HNC) diagnosis and identify. Head and neck cancer is a group of cancer that starts from the mucosal surfaces inside the head and neck (for example, inside the mouth, the nose, and the throat). Although whole-body (WB) PET has been widely used for the diagnosis and treatment of the HNC, the limited spatial resolution and sensitivity of WB PET lead to a large number of false-negative PET results in lymph nodes and make it unable to detect tumor involvement in lymph nodes smaller than 4-5 mm [42, 39].

This thesis will present the performance evaluation of a dedicated head and neck PET system based on cadmium zinc telluride (CZT), which is performed by Monte Carlo simulation in GATE (Geant4 Application for Tomographic Emission).

Chapter 2 presented the PET basic, different photon detection methods and different readout method in PET. The detailed design of two-panel head and neck PET

system is shown in Chapter 3 and chapter 4 reports the simulation results. Conclusion is in the chapter 5.

Chapter 2

Head and neck dedicated positron emission tomography

2.1 Positron emission tomography basic

Positron emission tomography (PET) is an noninvasive medical imaging modality that could achieve the in-vivo imaging mode. Before the PET scan, specific biological compound, such as fluorodeoxyglucose (FDG), should be injected into scanned organism [18]. PET could achieve the physiological process identification by observing the distribution of the biological compound.

An example of typical PET image acquisition procedure is depicted in the Figure 2.1. The injection of the biological compound (FDG used as the example in the Figure 2.1) is the first step of the whole procedure. Glucose is one of the energy sources for organisms, the distribution and concentration of glucose could indicate the

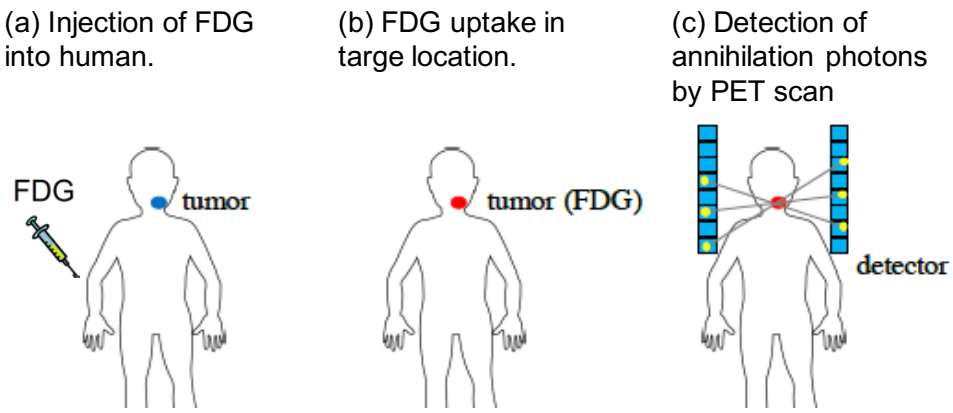

Figure 2.1: One example of human head and neck scan procedure (adapted from [18]).

metabolism activity rate of the organism. Since the FDG is a biological analog glucose, the distribution of the FDG also has the similar distribution pattern of glucose.

For the next step, the injected FDG will accumulated around the tumor due to the high metabolism rate of the cancer cell. Positrons would be emitted when the nucleus of ^{18}F atoms decay. The emitted Positron penetrates the tissue, loses energy and eventually annihilate into one pair of 511 keV photons with anti-parallel travel direction. The third step is to achieve the annihilation photons detection using PET scanner and obtain the tomographic image.

2.2 Different photon detection methods in PET

Basically, there are two main photon detection methods in PET 1) indirect detection method using scintillator detectors and 2) direct detection method using semiconductor detectors.

Property	LYSO	LSO	BGO	$LaBr_3$
Refractive index	1.81	1.82	2.15	1.9
Density	7.1	7.4	7.13	5.29
Peak emission (nm)	420	420	480	360
Light output (ph/MeV)	32000	31000	8500	65000
Decay time (ns)	41	40-47	300	15
Hygroscopic	no	no	no	yes

Table 2.1: Properties summary of LYSO, LSO, BGO and $LaBr_3$ (adapted from [18]).

For the scintillator, a large number of visible photons are induced in the scintillator due to the interaction with the high energy photons. Additional electronic readout devices (e.g. photo-detectors) are used to couple to the scintillator to convert the visible photons to the detectable electrical signal.

In PET applications, scintillators include Lutetium-yttrium oxyorthosilicate (LYSO), lutetium oxyorthosilicate (LSO), bismuth germanate (BGO) and lanthanum(III) bromide ($LaBr_3$) are the commonly used materials. Properties of these four scintillators are summarized in Table 2.1.

The commonly used photo-detectors in PET applications for visible light conversion are photomultiplier tube (PMT), avalanche photodiodes (APD) and silicon photomultiplier (SiPM). The properties of each photo-detector are summarized in Table 2.2. For all these three photo-detectors, the final output electric signal is orders of magnitude greater than the initial input electric signal (induced by the initial generated carriers).

For the direct detection method utilizing semiconductor, a large number of electrons could be induced in the semiconductor due to the interaction with high energy photon. No additional electrical readout devices would be needed. Commonly used

Property	PMT	APD	SiPM
Gain	10^6	50-1000	10^6
Rise time (ns)	1	5	1
Bias (V)	>1000	300-1000	30-80
Temperature sensitivity ($\%/_0C$)	< 1	3	1-8
Magnetic field sensitivity	yes	no	no

Table 2.2: Properties comparizon among three photo-detectors in PET: PMT, APD and SiPM (adapted from [18].)

semiconductors for radiation detection include cadmium telluride (CdTe) and cadmium zinc telluride (Cd0:9Zn0:1Te, henceforth simply CZT).

2.3 Different readout method in PET

For systems with small field of view, such as dedicated organ imaging and small animal imaging, spatial resolution and photon coincidence sensitivity are two of the most important properties [7, 43]. Spatial resolution determines the capability of resolving neighboring lesions and sensitivity determines the signal-to-noise ratio of the reconstructed image. To achieve high sensitivity, long crystals are utilized, and compact geometry is preferred so that a large solid angle of field of view (FOV) can be covered. However, systems with long crystals and compact geometry suffer from parallax error, which degrades the spatial resolution [30, 10]. In cylindrical scanners, for example, the radial spatial resolution component degrades gradually with the increase of the radial offset from the scanner center, and axial resolution is also degraded in the 3D acquisition. Fortunately, parallax error can be mitigated by using detectors with depth-of-interaction (DOI) capability [31, 1]. Figure 2.2 illustrates various readout crystal

methods. Different DOI detector configurations including, but not limited to, dual-ended readout, single-ended readout, side readout, and monolithic scintillator detector have been investigated for PET applications, as follows:

- Dual-ended readout uses two detectors that are coupled to both ends of crystals and DOI is estimated as the ratio of signal amplitudes of the two detectors [22]. In such a configuration, DOI is continuous, uniform and the resolution full-width at half-maximum (FWHM) can be smaller than 2 mm in 20-mm lutetium-yttrium oxyorthosilicate (LYSO) [15]. However, dual-ended readout doubles the number of detectors and readout channels, which increases the cost.

- Single-ended readout needs auxiliary techniques. For example, pulse shape discrimination is used to extract DOI from different layers of the crystal bar, which have different timing properties [6]. Another example is sharing light between neighboring crystals so that DOI is encoded by considering the extent of light dispersion [14]. DOI can also be decoded by using a light guide as the reflector on the other end of the crystal array [24]. The DOI resolution of single-ended readout is about 2 to 5 mm for 20-mm LSYO.

- Side readout reads signals from crystal lateral surfaces instead of end surfaces. In such a configuration, the DOI resolution equals to the scintillator crystal size, which is 5 to 7 mm [40, 44]. Higher DOI resolution can be achieved by reducing the crystal length, but more scintillator layers will be needed to maintain high sensitivity. Since the lateral surface area is larger than the ended surface area,

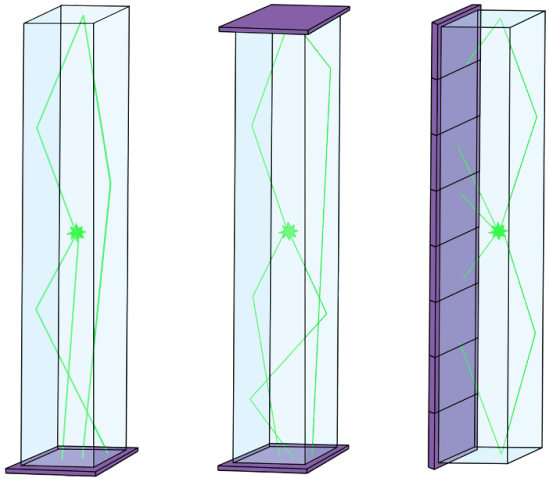

Figure 2.2: Illustration of single-ended, dual-ended, and side readout.

the cost of side readout is higher than dual-ended and single-ended readout. The detectors within crystal layers also lower the packing fraction.

A monolithic scintillator detector encodes DOI by calibration. Though it reduces the inter-crystal dead space and DOI resolution smaller than 2 mm can be achieved in 10-mm LYSO [27], the spatial resolution at the edges of the crystal is degraded, and the calibration of monolithic-scintillator-based detectors requires complicated procedures.

2.4 Head and Neck PET

PET and positron emission tomography/computed tomography (PET/CT) are commonly used for head and neck cancer (HNC) diagnosing, staging, treatment planning, assessing response to therapy [23, 11, 28]. Compared with CT, magnetic

resonance imaging (MRI), sonographic and histopathological findings, PET shows the highest sensitivity and specificity for detecting lymph node metastases of HNC [4]. However, the limited spatial resolution of whole-body PET (4 to 6 mm) leads to a large number of false-negative PET results in lymph nodes (e.g. 80% [42]) and makes it unable to detect tumor involvement in lymph nodes smaller than 4-5 mm [42, 39]. Dedicated head and neck (HN) acquisition protocol with longer scan time in HN bed position was introduced to improve the detection ability in HNC [39, 25]. It has advantages in detecting lymph nodes smaller than 15 mm compared to the standard protocol. However, no significant difference was reported between whole body (WB) and HN protocols in the evaluation of the primary tumor [25] and lymph nodes smaller than 4-5 mm are still not detectable [39]. A number of dedicated brain PET scanners are under development in various research labs [38, 20, 41, 13, 7]. However, their geometry and sensitivity is not optimized for HNC.

Chapter 3

Materials and Methods

3.1 System Geometry

Workflow of the hospital and ergonomic and cognitive needs of the patients are very important in design of a new clinical instrument for diagnosing HNC. Figure 3.1 illustrates three system geometries for dedicated head and neck system. Although a four-panel or ring design would allow for higher sensitivity, the proposed system was prototyped based on a two-panel design to demonstrate the clinical benefits of the high spatial resolution detectors in HNC PET imaging. Based on the human head size [17], the panel was set as 150×200 mm^2, and the distance between two panels was 200 mm. In addition, the required increase in inner diameter of a four-panel or ring design would limit the sensitivity gain ($<$ 1.5x assuming 35 cm inner diameter) and increase the cost significantly ($>$ 2x due to increased inner diameter). The two-panel design minimizes the amount of system in the line of sight of the patient to prevent claustrophobia and has

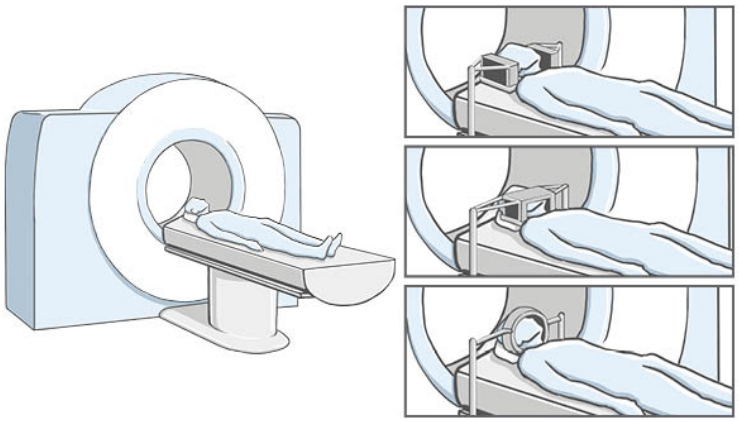

Figure 3.1: Three systems with two-panel, four-panel and full-ring geometries.

the flexibility for imaging organs and body parts that require more spatial resolution. The system panels are adjusted before the patient walks in the room and the system is controlled from a remote connection to reduce dose to the technologist. There will be no additional dose to the patient. The total system weight should be less than 400 lbs and should be able to be pushed/pulled with 30 lbs force (on the cart). The dimensions of the cart should be restricted to 80×50 cm^2. Figure 3.2 illustrates such a portable system.

3.2 Detecting material

Two different detector technology based on CZT [37, 34, 35, 36] and scintillator LYSO [26] were investigated for the dedicated system. For the LYSO system, the LYSO pixel size was 1×1 mm^2 and the crystal thickness was 20 mm. The LYSO detector module was previously developed in our lab (shown in Figure 3.3) based on 4×4 units

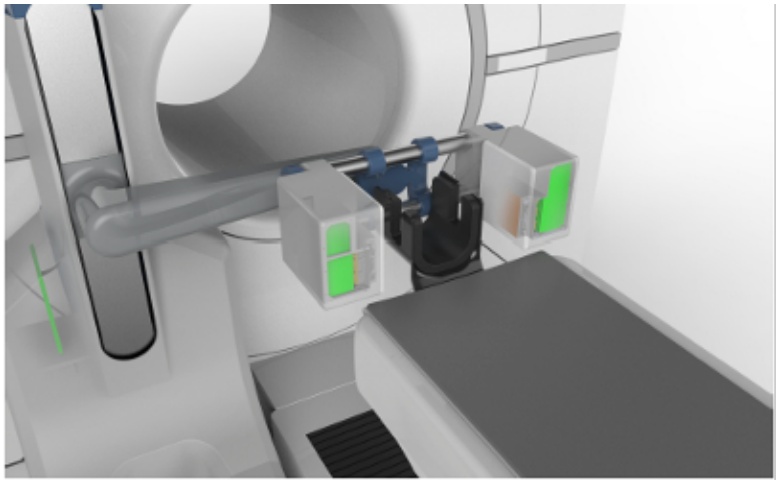

Figure 3.2: Illustration of a transportable two-panel dedicated head and neck cancer PET scanner integrated into the standard whole body PET/CT imaging workflow. The gantry is implemented to interface with the patient bed to image the patient right after the whole body PET scanning.

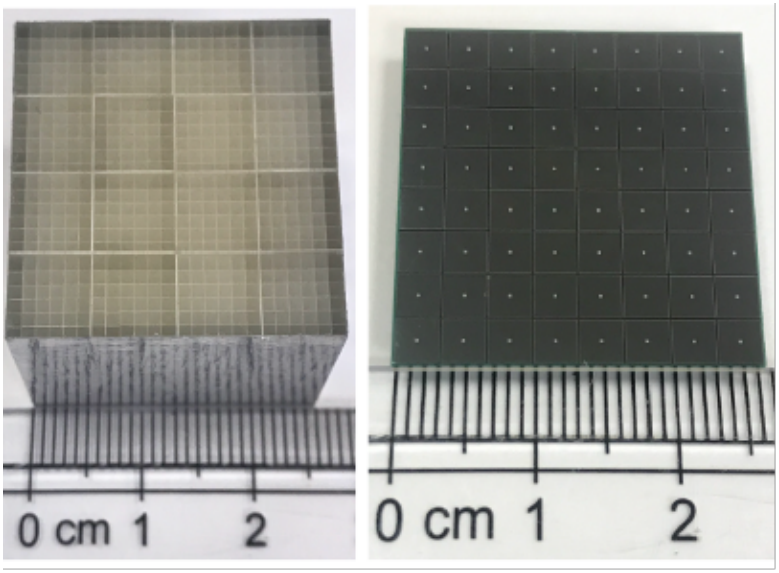

Figure 3.3: Left: The LYSO block contains 4×4 LYSO units. Right: The Hamamatsu A13361 3050AE-08 SiPM array contains 8×8 SiPM channels.

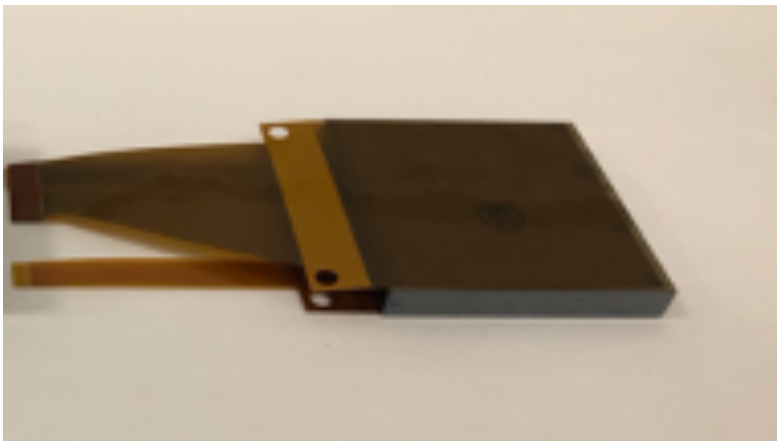

Figure 3.4: A 40×40×5 mm^3 CZT crystal assembled to flexible circuits. Each CZT crystal has 39 anode strips (100 µm width and 1 mm pitch), 38 steering electrode strips (400 µm width), and 8 cathode strips (4900 µm width and 5 mm pitch).

of 6×6 LYSO crystals from Epic Crystal, China. To extract the DOI information, two Hamamatsu S13361-3050AE-08 SiPM arrays were coupled to both ends of the LYSO with BC-630 optical grease (Saint-Gobain Crystals, USA). The fill factor was 86.5%. The energy resolution, time resolution, and DOI resolution were measured to be 15%, 600 ps, and 2.3 mm, respectively [19]. Monte Carlo simulation was performed in GATE (Geant4 Application for Tomographic Emission) to simulate the system performance. The time window and energy window for selecting coincidence events were 1.2 ns and [400, 620] keV, respectively.

For the CZT system, the crystal size was 40×40×5 mm^3. The CZT cross-strip detector (shown in Figure 3.4) was previously developed in our lab for a small animal PET system and the energy resolution, time resolution, and intrinsic spatial resolution were set to 2%, 8 ns, and 1×5×1 mm^3, respectively [3]. The time window was 15 ns and energy window was [490, 530] keV.

3.3 System sensitivity

The photon coincidence sensitivity was defined as the coincidence rate divided by the source activity. Generally only photons without scattering were used to constitute coincidences (P-P coincidence). To further improve sensitivity, multiple interaction photon events (MIPEs) have been recovered with different methods [3, 12, 33, 45]. In the proposed system, Compton kinematics [2, 46] was used to recover coincidences between annihilation photons that had a photoelectric event (P photon) and photons that had a Compton event before the photoelectric event (CP photon). For the rest of this chapter, these coincidences called P-CP coincidences. In Compton kinematics, the scattering angle can be computed by energy,

$$\theta_E = \arccos(1 - m_0c^2(\frac{1}{E_S} - \frac{1}{E_i})), \tag{3.1}$$

where E_i is the incident photon energy, E_S is the scattered photon energy, and m_0c^2 is the rest mass of an electron. For PET applications, $E_i = m_0c^2 = 511\ keV$.

The scattering angle can also be computed using the interaction position information,

$$\theta_P = \arccos(\frac{\vec{V}_i\vec{V}_s}{|V_i||V_s|}), \tag{3.2}$$

where $\vec{V}_i$ and $\vec{V}_s$ are the directions of incident and scattered photons. Figure 3.5 shows the principle to identify the Compton event in a P-CP coincidence [2]. To compare the sensitivity and MIPE recoverability of the two system and check the per-

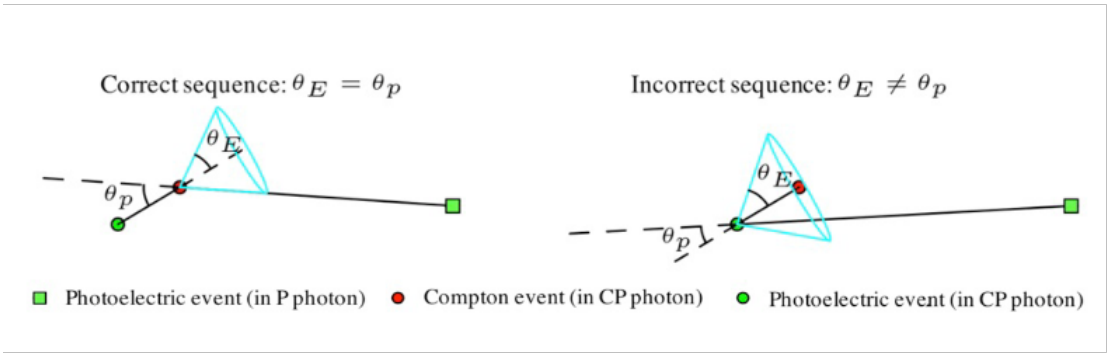

Figure 3.5: Using Compton kinematics to identify the Compton event in a P-CP coincidence. The sequence with a smaller θ_E - θ_P is picked up.

formance of Compton kinematics under high single rate, 10 point sources with different activities (7, 14, ..., 70 MBq) placed at the FOV center were simulated separately.

3.4 Image reconstruction

An 11-cm diameter and 12.6 cm long cylindrical phantom with uniform water attenuation was simulated. The background activity was 5700 Bq/cm^3 in the simulation. Hot spheres were put inside the phantom at the center slice, including a set of nine 3 mm diameter spheres, nine 4 mm diameter spheres, five 6 mm diameter spheres, and five 8mm diameter spheres as shown in Figure 3.6. The center-to-center distance between two neighboring spheres was twice the diameter of the spheres. The sphere to background ratio was 8:1. The simulation time was 10 min with 30 million coincidence events acquired. Images were reconstructed with a list-mode 3D maximum likelihood expectation maximization (MLEM) algorithm [29] through the gpurecon program [9]. Voxel size was 0.8×0.8×0.8 mm^3. Data corrections for scatter coincidence and random

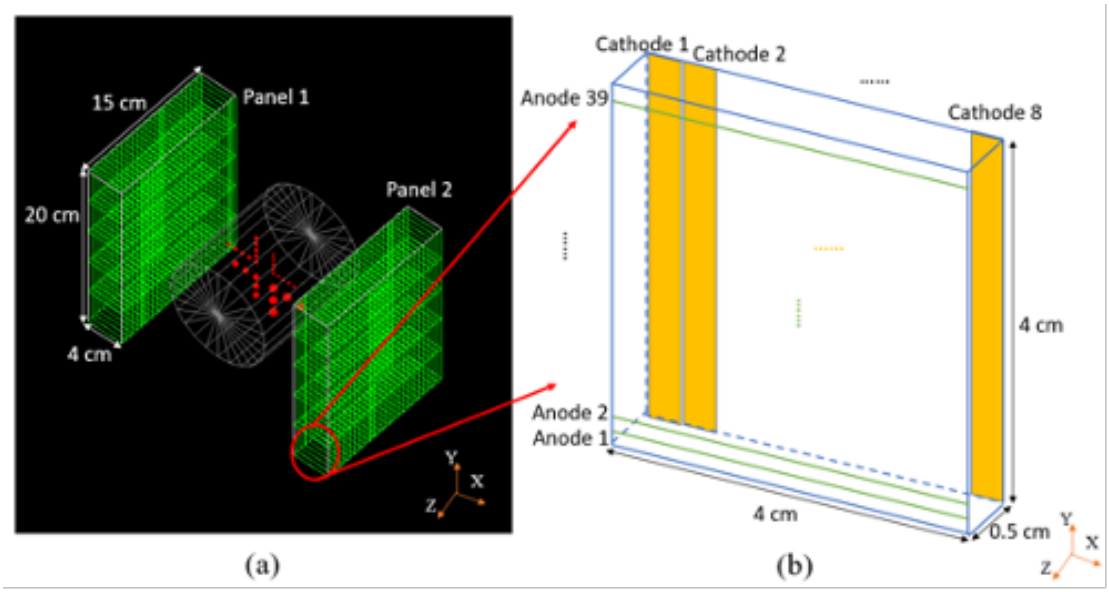

Figure 3.6: Schematic of the dual-panel dedicated system with simulated phantom.

coincidence were not applied. No regularization or post-reconstruction filter was used. The image quality is quantified by contrast recovery coefficient (CRC) and Contrast-to-noise-ratio (CNR):

$$CRC = \frac{\frac{C_{hot}}{C_{bkg}} - 1}{\frac{a_{hot}}{a_{bkg}} - 1}, \tag{3.3}$$

$$CNR = \frac{C_{hot} - C_{bkg}}{\sigma_{bkg}}, \tag{3.4}$$

where C_{hot} and C_{bkg} are the average voxel value in a hot sphere and background region of interest (ROI), respectively, a_{hot} and a_{bkg} are the ground-truth concentration activity, and a_{bkg} is the standard deviation of the voxel values in the background ROI.

Previously several approaches to reducing limited-angle artifacts without de-

tector rotation have been studied for breast-dedicated PET systems, such as time-of-flight (TOF) image reconstruction and image-based modeling of point-spread-function (PSF) deformation [32, 16, 21]. In the proposed system, limited angle artifact can be addressed using a penalized maximum-likelihood (PML) reconstruction method similar to prior image constrained compressed sensing (PICCS) [8]. The prior image is pre-reconstructed from a whole-body PET scan. PML is then performed with a regularization term that penalizes the dissimilarity between the image to be reconstructed (the target image) and the prior image. An image-based resolution model is incorporating into the regularization term considering the limited spatial resolution of the whole-body scanner.

Chapter 4

Simulation results

4.1 Spatial resolution and sensitivity with LYSO and CZT

The in-panel and orthogonal-panel spatial resolution of CZT and LYSO systems based on only P-P coincidences and both P-P and P-CP coincidences are shown in Table 1. The results indicated that CZT had a better spatial resolution than LYSO, and incorporating P-CP coincidences for image reconstruction would slightly deteriorate the spatial resolution.

The sensitivity and P-CP coincidences recovery accuracy of the CZT and LYSO

Spatial resolution	P-P coincidence	P-P and P-CP coincidence
CZT in-panel	0.56 mm	0.58 mm
CZT orthogonal panel	0.71 mm	0.74 mm
LYSO in-panel	0.62 mm	0.7 mm
LYSO orthogonal panel	1.31 mm	1.4 mm

Table 4.1: Point source spatial resolution of the CZT and LYSO system.

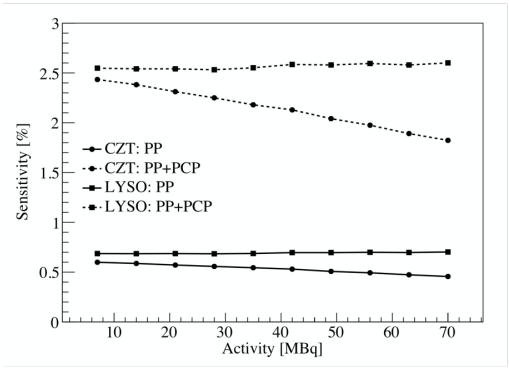

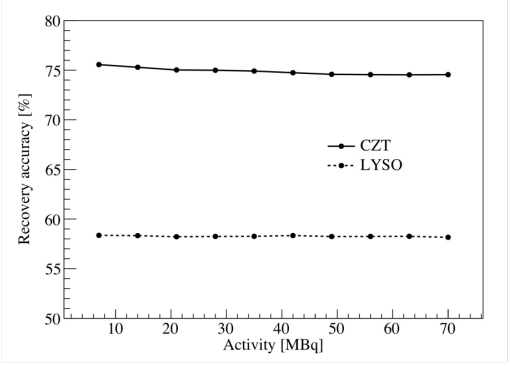

Figure 4.1: The sensitivity (left) and P-CP coincidences recovery accuracy (right) of the CZT and LYSO systems under different source activities.

systems under different source activities is shown in Figure 4.1. At 7 MBq, the sensitivity of the CZT and LYSO systems are 0.60% and 0.69%, and it increased to 2.43% and 2.55% respectively after recovering MIPEs. The results showed that with a 40 mm crystal thickness, the CZT system could achieve similar sensitivity as the LYSO system. After recovering MIPEs, the sensitivity of both systems improved approximately 3 times, which indicated the importance of MIPE recovery. Due to the poor time resolution, the P-CP sensitivity of the CZT system decreased 25.5% with the increase of activity from 7 MBq to 70 MBq. The results also showed that given a source activity, the recovery accuracy of the CZT system was about 20% higher than LYSO, and the recovery accuracy was not affected by the source activity.

4.2 Performance evaluation in image reconstruction

The transverse slices and sagittal slices from reconstructed images for the cylindrical phantom with hot spheres (as shown in Figure 3.6) are shown in Figure 4.2 and

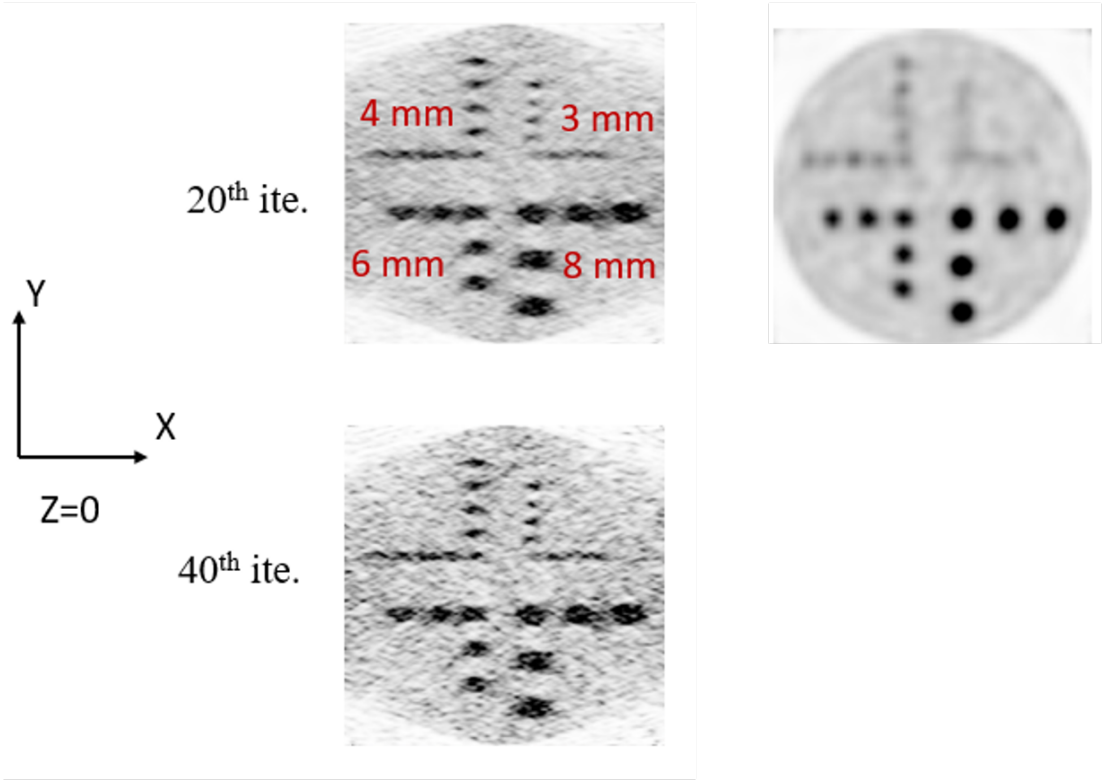

Figure 4.2: Transverse slices (Z=0) from reconstructed images for the cylindrical phantom with hot spheres. The images are transverse slices from target images reconstructed from the dual-panel high-spatial-resolution PET scan of the phantom. The left images are from the ML reconstruction without any regularization. The right image is a transverse slice from the whole-body PET scan of the phantom using GE discovery MI model. Each image has 220 × 220 pixels, with the size of each pixel being 0.5 mm × 0.5 mm.

Figure 4.3, respectively. The images at 20th and 40th iterations are both shown in the figures. Small hot spheres (3 mm and 4 mm in diameter) are better resolved in the dedicated system compared to whole-body system. The geometry of the whole-body scanner used in simulation was referred from the Discovery MI 4-ring PET scanner (GE Healthcare). The background and hot spheres are both elongated, as shown in Figure 4.2. With PML image reconstruction, the limited angel artifacts can be mitigated.

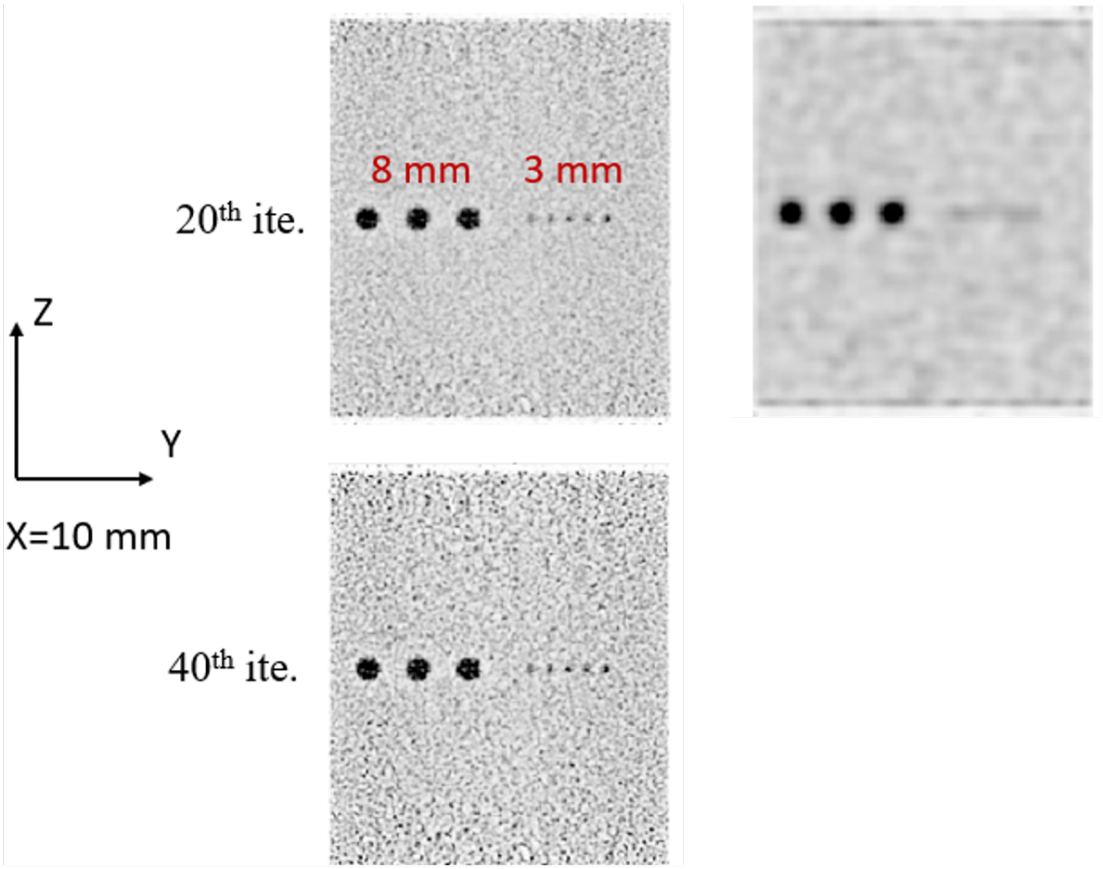

Figure 4.3: Sagittal slices (X=10 mm) through 3-mm and 8-mm diameter hot spheres from reconstructed images for the cylindrical phantom with hot spheres. The left images are sagittal slices from target images reconstructed from the dual-panel high-spatial-resolution PET scan of the phantom. The images are from the ML reconstruction without any regularization. The right image is a sagittal slice from the prior image reconstructed from the whole-body PET scan of the phantom. Each image has 220 (Y) $\times$ 260 (Z) pixels, with the size of each pixel being 0.5 mm $\times$ 0.5 mm.

Chapter 5

Conclusion

We studied the design considerations for a dedicated HNC PET scanner. For detecting material, CZT shows comparable sensitivity and superior spatial resolution when compared with LYSO, which indicates the potential of applying CZT to HNC imaging. For system geometry, even though the full geometry (full-ring) designs achieve better sensitivity, it comes with a doubled cost, due to the doubled numbers of detectors. Further, panel-based designs have the flexibility to adjust the panel distance for other organs. Finally, it is important to consider the patients' comfort in such a compact geometry design, and two-panel geometry can achieve better spatial resolution than a whole-body PET system. A dedicated high spatial resolution system can detect tumor involvement in small lymph nodes (< 10 mm) and alleviate the challenges associated with identifying tumor boundaries in current whole-body PET scanner. Recovering the first interaction in MIPEs using Compton Kinematics relies on both recorded energy and position to determine the sequence of interactions and create the line of response. Using

CZT crystals with high-energy resolution and high spatial resolution in three dimensions, multiple interaction photon events can recover with high accuracy. This technique will have substantial impact on sensitivity and contrast recovery of the system.

Bibliography

[1] A prototype PET scanner with DOI-encoding detector, author=Yang, Yongfeng and Wu, Yibao and Qi, Jinyi and James, Sara St and Du, Huini and Dokhale, Purushottam A and Shah, Kanai S and Farrell, Richard and Cherry, Simon R, journal=Journal of Nuclear Medicine, volume=49, number=7, pages=1132–1140, year=2008, publisher=Soc Nuclear Med.

[2] Shiva Abbaszadeh, Garry Chinn, and Craig S Levin. Positioning true coincidences that undergo inter-and intra-crystal scatter for a sub-mm resolution cadmium zinc telluride-based PET system. *Physics in Medicine & Biology*, 63(2):025012, 2018.

[3] Shiva Abbaszadeh, Yi Gu, Paul D Reynolds, and Craig S Levin. Characterization of a sub-assembly of 3D position sensitive cadmium zinc telluride detectors and electronics from a sub-millimeter resolution PET system. *Physics in Medicine & Biology*, 61(18):6733, 2016.

[4] Stefan Adams, Richard P Baum, Tankred Stuckensen, Klaus Bitter, and Gustav Hör. Prospective comparison of 18 F-FDG PET with conventional imaging modal-

ities (CT, MRI, US) in lymph node staging of head and neck cancer. *European journal of nuclear medicine*, 25(9):1255–1260, 1998.

[5] Christopher E Bauer, Julie Brefczynski-Lewis, Gary Marano, Mary-Beth Mandich, Alexander Stolin, Peter Martone, James W Lewis, Gangadhar Jaliparthi, Raymond R Raylman, and Stan Majewski. Concept of an upright wearable positron emission tomography imager in humans. *Brain and behavior*, 6(9):e00530, 2016.

[6] Eric Berg, Emilie Roncali, Maciej Kapusta, Junwei Du, and Simon R Cherry. A combined time-of-flight and depth-of-interaction detector for total-body positron emission tomography. *Medical physics*, 43(2):939–950, 2016.

[7] Kent C Burr, Adrian Ivan, Donald E Castleberry, James W LeBlanc, Kanai S Shah, and RAFR Farrell. Evaluation of a prototype small-animal PET detector with depth-of-interaction encoding. *IEEE Transactions on Nuclear Science*, 51(4):1791–1798, 2004.

[8] Guang-Hong Chen, Jie Tang, and Jiang Hsieh. Temporal resolution improvement using PICCS in MDCT cardiac imaging. *Medical physics*, 36(6Part1):2130–2135, 2009.

[9] Jingyu Cui, Guillem Pratx, Bowen Meng, and Craig S Levin. Distributed MLEM: An iterative tomographic image reconstruction algorithm for distributed memory architectures. *IEEE transactions on medical imaging*, 32(5):957–967, 2013.

[10] PA Dokhale, RW Silverman, Kanai S Shah, R Grazioso, Richard Farrell, J Glodo,

MA McClish, G Entine, VH Tran, and Simon R Cherry. Performance measurements of a depth-encoding PET detector module based on position-sensitive avalanche photodiode read-out. *Physics in Medicine & Biology*, 49(18):4293, 2004.

[11] Susanne-Martina Eschmann, Frank Paulsen, Matthias Reimold, Helmut Dittmann, Stefan Welz, Gerald Reischl, Hans-Juergen Machulla, and Roland Bares. Prognostic impact of hypoxia imaging with 18F-misonidazole PET in non-small cell lung cancer and head and neck cancer before radiotherapy. *Journal of nuclear medicine*, 46(2):253–260, 2005.

[12] John E Gillam, Paola Solevi, Josep F Oliver, Chiara Casella, Matthieu Heller, Christian Joram, and Magdalena Rafecas. Sensitivity recovery for the AX-PET prototype using inter-crystal scattering events. *Physics in Medicine & Biology*, 59(15):4065, 2014.

[13] Kuang Gong, Stan Majewski, Paul E Kinahan, Robert L Harrison, Brian F Elston, Ravindra Manjeshwar, Sergei Dolinsky, Alexander V Stolin, Julie A Brefczynski-Lewis, and Jinyi Qi. Designing a compact high performance brain PET scanner—simulation study. *Physics in Medicine & Biology*, 61(10):3681, 2016.

[14] Mikiko Ito, Jae Sung Lee, Min-Jae Park, Kwang-Souk Sim, and Seong Jong Hong. Design and simulation of a novel method for determining depth-of-interaction in a PET scintillation crystal array using a single-ended readout by a multi-anode PMT. *Physics in Medicine & Biology*, 55(13):3827, 2010.

[15] Zhonghua Kuang, Xiaohui Wang, Cheng Li, Xinhan Deng, Kai Feng, Zhanli Hu, Xin Fu, Ning Ren, Xianming Zhang, Yunfei Zheng, et al. Performance of a high-resolution depth encoding PET detector using barium sulfate reflector. *Physics in Medicine & Biology*, 62(15):5945, 2017.

[16] Eunsin Lee, Matthew E Werner, Joel S Karp, and Suleman Surti. Design optimization of a time-of-flight, breast PET scanner. *IEEE transactions on nuclear science*, 60(3):1645–1652, 2013.

[17] Jin-hee Lee, Su-Jeong Hwang Shin, and Cynthia L Istook. Analysis of human head shapes in the united states. *International Journal of Human Ecology*, 7(1):77–83, 2006.

[18] Mohan Li. Design study of a two-panel head-and-neck cancer dedicated position emission tomography system. 2018.

[19] Mohan Li and Shiva Abbaszadeh. Depth-of-interaction study of a dual-readout detector based on TOFPET2 application-specific integrated circuit. *Physics in Medicine & Biology*, 64(17):175008, 2019.

[20] S Majewski, J Proffitt, J Brefczynski-Lewis, A Stolin, AG Weisenberger, W Xi, and R Wojcik. HelmetPET: A silicon photomultiplier based wearable brain imager. In *2011 IEEE Nuclear Science Symposium Conference Record*, pages 4030–4034. IEEE, 2011.

[21] Samuel Matej, Yusheng Li, Joseph Panetta, Joel S Karp, and Suleman Surti. Image-

based modeling of PSF deformation with application to limited angle PET data. *IEEE transactions on nuclear science*, 63(5):2599–2606, 2016.

[22] WW Moses and Stephen E Derenzo. Design studies for a PET detector module using a PIN photodiode to measure depth of interaction. *IEEE Transactions on Nuclear Science*, 41(4):1441–1445, 1994.

[23] B Nowak, E Di Martino, S Jänicke, U Cremerius, G Adam, M Zimny, P Reinartz, and U Büll. Diagnostic evaluation of malignant head and neck cancer by F-18-FDG PET compared to CT/MRI. *Nuklearmedizin*, 38(08):312–318, 1999.

[24] Marco Pizzichemi, Gianluca Stringhini, Tahereh Niknejad, Zile Liu, Paul Lecoq, Stefaan Tavernier, J Varela, M Paganoni, and Etiennette Auffray. A new method for depth of interaction determination in PET detectors. *Physics in Medicine & Biology*, 61(12):4679, 2016.

[25] Rosana S Rodrigues, Fernando A Bozza, Paul E Christian, John M Hoffman, Regan I Butterfield, Carl R Christensen, Marta Heilbrun, Richard H Wiggins, Jason P Hunt, Brandon G Bentz, et al. Comparison of whole-body PET/CT, dedicated high-resolution head and neck PET/CT, and contrast-enhanced CT in preoperative staging of clinically M0 squamous cell carcinoma of the head and neck. *Journal of Nuclear Medicine*, 50(8):1205–1213, 2009.

[26] Gregory Romanchek, Yuli Wang, Harsha Marupudi, and Shiva Abbaszadeh. Perfor-

mance of Optical Coupling Materials in Scintillation Detectors Post Temperature Exposure. *Sensors*, 20(21):6092, 2020.

[27] Dennis R Schaart, Herman T van Dam, Stefan Seifert, Ruud Vinke, Peter Dendooven, Herbert Löhner, and Freek J Beekman. A novel, SiPM-array-based, monolithic scintillator detector for PET. *Physics in Medicine & Biology*, 54(11):3501, 2009.

[28] David L Schwartz, Eric Ford, Joseph Rajendran, Bevan Yueh, Marc D Coltrera, Jeffery Virgin, Yoshimi Anzai, David Haynor, Barbara Lewellyn, David Mattes, et al. DG-PET/CT imaging for preradiotherapy staging of head-and-neck squamous cell carcinoma. *International Journal of Radiation Oncology* Biology* Physics*, 61(1):129–136, 2005.

[29] Lawrence A Shepp and Yehuda Vardi. Maximum likelihood reconstruction for emission tomography. *IEEE transactions on medical imaging*, 1(2):113–122, 1982.

[30] Sara St James, Yongfeng Yang, Yibao Wu, Richard Farrell, Purushottam Dokhale, Kanai S Shah, and Simon R Cherry. Experimental characterization and system simulations of depth of interaction PET detectors using 0.5 mm and 0.7 mm LSO arrays. *Physics in Medicine & Biology*, 54(14):4605, 2009.

[31] Jennifer R Stickel and Simon R Cherry. High-resolution PET detector design: modelling components of intrinsic spatial resolution. *Physics in Medicine & Biology*, 50(2):179, 2004.

[32] Suleman Surti and Joel S Karp. Design considerations for a limited angle, dedicated breast, TOF PET scanner. *Physics in Medicine & Biology*, 53(11):2911, 2008.

[33] Ashwin A Wagadarikar, Adrian Ivan, Sergei Dolinsky, and David L McDaniel. Sensitivity improvement of time-of-flight (ToF) PET detector through recovery of compton scattered annihilation photons. *IEEE Transactions on Nuclear Science*, 61(1):121–125, 2013.

[34] Yuli Wang, Ryan Herbst, and Shiva Abbaszedeh. Back-end readout electronic design and initial results: a head-and-neck dedicated PET system based on CZT. In *Medical Imaging 2021: Physics of Medical Imaging*, volume 11595, page 1159510. International Society for Optics and Photonics, 2021.

[35] Yuli Wang, Yingjie Li, Fei Yi, Junyu Li, Siwei Xie, Qiyu Peng, and Jianfeng Xu. Two-crossed-polarizers based optical property modulation method for ionizing radiation detection for positron emission tomography. *Physics in Medicine & Biology*, 64(13):135017, 2019.

[36] Yuli Wang, Zehao Li, and Jianfeng Xu. Investigation of Pockels effect in optical property modulation-based radiation detection method for positron emission tomography. In *Medical Imaging 2019: Biomedical Applications in Molecular, Structural, and Functional Imaging*, volume 10953, page 1095306. International Society for Optics and Photonics, 2019.

[37] Yuli Wang, Li Tao, Shiva Abbaszadeh, and Craig Levin. Further investigations of a

radiation detector based on ionization-induced modulation of optical polarization. *Physics in Medicine & Biology*, 66(5):055013, 2021.

[38] Seiichi Yamamoto, Manabu Honda, Tutomu Oohashi, Keiji Shimizu, and Michio Senda. Development of a brain PET system, PET-Hat: a wearable PET system for brain research. *IEEE Transactions on Nuclear Science*, 58(3):668–673, 2011.

[39] Yuka Yamamoto, Terence Z Wong, Timothy G Turkington, Thomas C Hawk, and R Edward Coleman. Head and neck cancer: dedicated FDG PET/CT protocol for detection—phantom and initial clinical studies. *Radiology*, 244(1):263–272, 2007.

[40] Taiga Yamaya, Naoki Hagiwara, Takashi Obi, Tomoaki Tsuda, Keishi Kitamura, Tomoyuki Hasegawa, Hideaki Haneishi, Naoko Inadama, Eiji Yoshida, and Hideo Murayama. Preliminary resolution performance of the prototype system for a 4-layer DOI-PET scanner: jPET-D4. *IEEE transactions on nuclear science*, 53(3):1123–1128, 2006.

[41] Taiga Yamaya, Eiji Yoshida, Hideaki Tashima, Naoko Inadama, Tetsuya Shinaji, Hidekatsu Wakizaka, Munetaka Nitta, Shusaku Tazawa, Tetsuya Suhara, and Yasuhisa Fujibayashi. First prototype of a compact helmet-chin PET for high-sensitivity brain imaging. *Journal of Nuclear Medicine*, 56(supplement 3):317–317, 2015.

[42] Yutaka Yamazaki, Masaaki Saitoh, Ken-ichi Notani, Kanchu Tei, Yasunori Totsuka, Shu-ichi Takinami, Kakuko Kanegae, Masayuki Inubushi, Nagara Tamaki, and

Yoshimasa Kitagawa. Assessment of cervical lymph node metastases using FDG-PET in patients with head and neck cancer. *Annals of nuclear medicine*, 22(3):177–184, 2008.

[43] Yongfeng Yang, Julien Bec, Jian Zhou, Mengxi Zhang, Martin S Judenhofer, Xiaowei Bai, Kun Di, Yibao Wu, Mercedes Rodriguez, Purushottam Dokhale, et al. A prototype high-resolution small-animal PET scanner dedicated to mouse brain imaging. *Journal of Nuclear Medicine*, 57(7):1130–1135, 2016.

[44] Jung Yeol Yeom, Ruud Vinke, and Craig S Levin. Side readout of long scintillation crystal elements with digital SiPM for TOF-DOI PET. *Medical physics*, 41(12):122501, 2014.

[45] Eiji Yoshida, Hideaki Tashima, and Taiga Yamaya. Sensitivity booster for DOI-PET scanner by utilizing Compton scattering events between detector blocks. *Nuclear Instruments and Methods in Physics Research Section A: Accelerators, Spectrometers, Detectors and Associated Equipment*, 763:502–509, 2014.

[46] Hengquan Zhang, Yuli Wang, Jinyi Qi, and Shiva Abbaszadeh. Penalized maximum-likelihood reconstruction for improving limited-angle artifacts in a dedicated head and neck PET system. *Physics in Medicine & Biology*, 65(16):165016, 2020.